Department of Physics and Astronomy
University of Heidelberg

Bachelor Thesis in Physics
submitted by

Jonathan Lommen

born in Konstanz (Germany)

2011

Erstgutachter: Prof. Dr. Klaus Blaum
Zweitgutachter: PD Dr. Yuri Litvinov

Reference Masses for Precision Mass Spectrometry

Design and Implementation of a Pierce Geometry to the Cluster Ion Source at ISOLTRAP

This Bachelor Thesis has been carried out by Jonathan Lommen at the
Max-Planck Institute for Nuclear Physics in Heidelberg and at ISOLTRAP at CERN
under the supervision of
Prof. Dr. Klaus Blaum and Dr. Susanne Kreim

Zusammenfassung

Am Massenspektrometer ISOLTRAP stehen Kohlenstoff-Cluster zur Verfügung, denen vor allem im Bereich schwerer Massen ($m \geq 200\,\mathrm{u}$) große Bedeutung zukommt. In diesem Massenbereich wird die Messunsicherheit zunehmend durch die Differenz zwischen Referenzmasse und gesuchter Ionenmasse dominiert. Durch die Verwendung der Cluster anstatt des üblichen ^{133}Cs, verringert sich dieser Unterschied. Die Kohlenstoff-Cluster werden mit einer Laserionenquelle erzeugt, deren Funktionstüchtigkeit im Rahmen dieser Arbeit verbessert wurde. Es wurde zum einen die Fluktuation der Zählrate als Funktion der Laserenergie untersucht. Die Energiedichte am Target wurde durch den Einbau eines Teleskops in den Strahlgang erhöht, was zu einer schmaleren Energieverteilung der Ionen führte. Des Weiteren konnte durch exaktes Einstellen von Zeitpunkt und Dauer einer gepulsten Kavität ein Energiebereich aus der Ionenwolke ausgewählt werden, in welchem die Zählrate konstant bleibt. Um ideale Startbedingungen während und nach der Laserablation zu gewährleisten, wurde eine neue Extraktion entwickelt. Die Werkstücke wurden nach erstellten technischen Zeichnungen gefertigt. Zum anderen wurde durch eine Präzisionsmassenmessung von ^{208}Fr dessen bisheriger Fehler um fast eine Größenordnung auf unter 7 keV verringert.

Abstract

At the mass spectrometer ISOLTRAP carbon clusters are provided which are of particular importance in higher mass ranges ($m \geq 200\,\mathrm{u}$). In this mass range the measurement uncertainty is increasingly dominated by the difference of the reference mass and the mass of the ion of interest. Using carbon clusters instead of the common ^{133}Cs, this difference decreases. The carbon clusters are produced in a laser ion source which has been improved in the frame of this work. The fluctuations of the count rate have been investigated as a function of the laser energy. Furthermore, the energy density at the target has been increased by implementation of a telescope into the laser beam line, which leads to a more narrow energy distribution of the ions. Through the exact adjustment of timing and length of a pulsed cavity an energy range with constant count rate could be selected. In order to provide ideal starting conditions during and after the laser ablation, a new extraction has been designed. The parts were manufactured according to technical drawings which have been produced. Moreover, performing a precision mass measurement, the uncertainty of ^{208}Fr was decreased almost one order of magnitude to less than 7 keV.

Contents

List of Figures

List of Tables

1. Introduction

Penning-trap mass-spectrometry is a common tool in physics and chemistry to determine the mass of both stable elements or molecules and radioactive nuclei all over the chart of nuclides. At the tandem Penning-trap mass spectrometer ISOLTRAP, the mass of extremely short-lived isotopes is measured. This is done by storing charged particles in a magnetic field B. The characteristic cyclotron frequency $\omega_c = {}^{qB}/_{m}$ contains the information about the mass m, where q is the charge of the particle. Usually, the magnetic field cannot be measured very precisely wherefore it is bypassed by measuring a well-known reference mass. Then, the ratio of the two frequencies yields the unknown mass. In the case of carbon, no uncertainty is introduced since the atomic mass unit is defined by ${}^{1}/_{12}$th of the mass of a ^{12}C atom. At ISOLTRAP, carbon clusters can be produced by an implemented laser ion source. The carbon clusters occur with masses up to 200 u and more. Thus, they are the ideal choice of a reference mass especially for mass ranges where no other stable elements are easily available.
With the present laser ion source at ISOLTRAP, a stable rate of laser-ablated ions has been difficult to achieve. To this end, modifications of the setup have been performed. An appropriate extraction electrode with a Pierce electrode-like shape has been designed and is ready for the implementation. The shape was analysed by simulations with the code of SIMION® to take into account the different starting conditions of the ions as compared to the original solution by Pierce [1]. The laser focus of the 532 nm Nd:YAG laser has also been improved by implementing a telescope into the laser beam line. This increases the energy density at the target which yields a higher count rate and thereby helps to reach stable working conditions at low laser powers. It also improves the starting conditions because the initial energy spread of the ion beam is minimised. Both modifications work well elsewhere [2]. In general, the energy distribution of the ablated ions is very broad. This causes problems during further preparation of the ions. Thus, a pulsed cavity in front of the first Penning-trap was used to reduce the energy spread by appropriate length and timing of the pulse.
At first, Penning-trap mass spectrometry and the ISOLTRAP experiment will be presented in chapter 2. Along a recent mass measurement of ^{208}Fr, the achievable precision in the heavy mass range and the influence of the reference mass on the result will be discussed. Chapter 3 deals with the setup of the laser ion source and the principles of laser ablation. The results concerning the count-rate fluctuations, the implementation of the telescope together with the foregoing focus measurements, and finally, the energy selection are presented. The design and theory of the new electrode are described jointly with the simulations in chapter 4. The conclusion will summarise the work performed during this thesis.

2. The Penning-trap Mass Spectrometer ISOLTRAP

The ISOLTRAP experiment located at the ISOLDE facility at CERN on the border of France and Switzerland is a tandem Penning-trap mass spectrometer which is able to determine the mass of short-lived nuclei with a relative uncertainty of 1×10^{-8}. Since the mass of a nucleus is coupled directly to its binding energy, by means of mass spectroscopy deeper insight into the composition of matter can be obtained. Among others, the synthesis of matter in stars and super novae can be understood through mass measurements. It also makes it possible to gain insights into particle and neutrino physics [3].
In this chapter, the setup of ISOLDE and ISOLTRAP will be discussed. Then, the the motion of a charged particle in a Penning trap and the principle of a time-of-flight measurement will be explained. The mass of ^{208}Fr is presented which was determined in a recent measurement. Finally, a short discussion of the uncertainty of mass measurements at ISOLTRAP will be given which leads to carbon clusters as the reference mass of choice since they have no intrinsic uncertainty.

2.1. The Setup of ISOLDE and ISOLTRAP

The on-line isotope separator ISOLDE produces radioactive ion beams by irradiating different target materials with a 1.4 GeV proton beam usually every 1.2 s. Neutral particles diffuse out of the heated target and become ionised by surface or laser ionisation. The ions are accelerated up to 60 keV and mass separated in a magnetic field by either the GPS (General Purpose Separator) or the HRS (High Resolution Separator). The mass resolution of the latter is $m/\delta m = 3000 - 4500$ [4]. An overview of the ISOLDE experimental hall is provided in fig. 2.1. ISOLTRAP is located at the end of the central beam line.

This quasi-continuous ion beam is transferred to ISOLTRAP where it is cooled and bunched, isobars are separated, and at last the mass is determined in a Penning-trap. An schematic view of the ISOLTRAP experiment is given in fig. 2.2. The cooling and bunching is performed by the radio-frequency quadrupole (RFQ), where the ions collide with helium gas and loose kinetic energy. Electrostatic fields provide the bunching. Then, the ions pass the isobar separator and the first cylindrical Penning trap, where the beam is cleaned of isobaric contamination and prepared for the actual measurement in the second, hyperbolic Penning trap. There, the actual measurement is performed. The trapped particles are excited by a radio-frequency field and then ejected from the trap. Their time-of-flight to a detector is measured which is directly connected to the energy

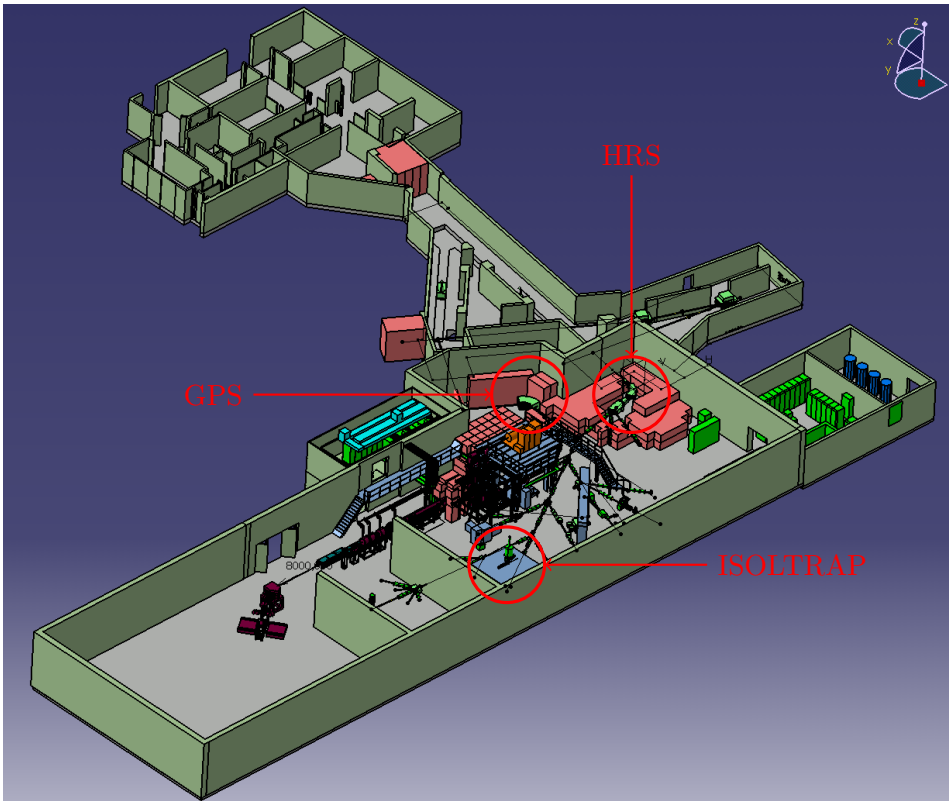

Figure 2.1.: Overview of the experimental hall of ISOLDE. ISOLTRAP is located at the end of the central beam line.

pickup in the trap. In conjunction with a reference mass measurement, the time-of-flight detection method is used to determine the mass.
ISOLTRAP is equipped with two off-line reference ion sources. An alkali ion source in front of the RFQ and a laser ion source after the isobaric separator from which palladium, cadmium and carbon clusters can be obtained. The latter is of special interest within this work.

2.2. Principles of Mass Measurements in a Penning Trap

A particle with a charge q moving through a homogeneous magnetic field $\vec{B} = B\vec{\hat{z}}$ experiences a force perpendicular to its original direction. This causes a circular orbit with a frequency of

$$\omega_c = \frac{q}{m} B\,, \tag{2.1}$$

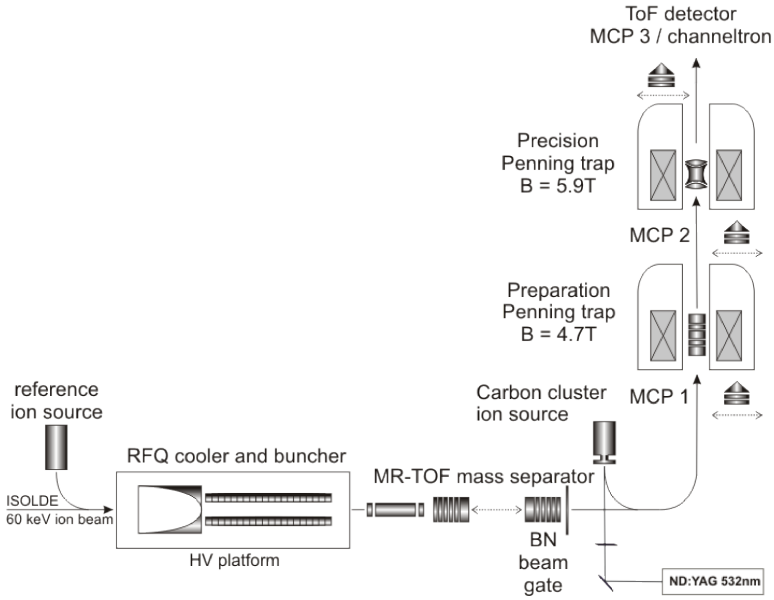

Figure 2.2.: The setup of ISOLTRAP in a schematic view. The laser ion source is located between the isobaric separator and the preparation trap.

the cyclotron frequency. In this way, the particle is radially bound. To confine it in all three dimensions, an axial confinement can be achieved by superimposing an electrostatic quadrupole potential of the form

$$\Phi(\rho, z) = \frac{U_0}{2d^2}\left(z^2 - \frac{\rho^2}{2}\right), \tag{2.2}$$

which can be realised by different, axially symmetric electrode configurations. Then, U_0 is the voltage applied to the electrodes, $\rho = \sqrt{x^2 + y^2}$ the radial distance and d a geometry factor. This configuration is called a Penning trap. In case of a hyperbolic trap, the electrodes are shaped like the equipotential lines of the potential and the voltage U_0 is applied between the hyperbolic ring electrodes and end caps as shown in fig. 2.3.

The particle experiences the force

$$\vec{F} = m\ddot{\vec{x}} = q\left(-\nabla\Phi(\rho, z) + \dot{\vec{x}} \times \vec{B}\right), \tag{2.3}$$

from which the equations of motion can be formulated in cylindrical coordinates

$$\ddot{\rho} = \frac{q}{m}\left(E_\rho + \dot{\rho} \times \vec{B}\right) \tag{2.4}$$

$$\ddot{z} = \frac{qE_z}{m} z\,. \tag{2.5}$$

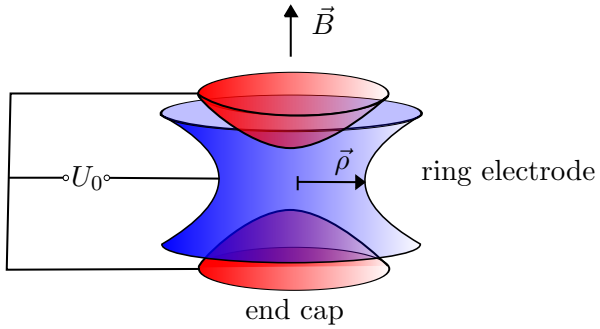

Figure 2.3.: Hyperbolic Penning trap. The ring electrode is four-fold segmented in order to apply excitation potentials (not shown).

The last equation is a harmonic oscillator in z-direction with the frequency of the *axial* motion

$$\omega_z = \sqrt{\frac{qU_0}{md}}\,. \tag{2.6}$$

The radial motion consists of two independent circular motions – a high-frequency motion called *modified cyclotron* motion and the so-called *magnetron* motion with a low frequency. The frequencies are

$$\omega\pm = \frac{\omega_c}{2} \pm \sqrt{\frac{\omega_c^2}{4} - \frac{\omega_z^2}{2}}\,, \tag{2.7}$$

where the "$-$" denotes the magnetron motion and the "$+$" the modified cyclotron motion. From this, it follows that

$$\omega_c = \omega_+ + \omega_-\,. \tag{2.8}$$

2.2.1. The Time-of-Flight (ToF) Measurement

In general, an isobarically pure beam reaches the precision Penning trap, where the mass is determined. There, a bipolar rf-field on ω_- is applied and increases the energy in this eigenmode [5]. This frequency is not required to be well-known since it is to first order mass independent. Subsequently, a quadrupolar rf-field excites the ions on ω_c and by use of eqn. (2.8) energy is converted from the magnetron motion into the modified cyclotron motion. Only if the true ω_c of the particle is hit, the energy transfer is maximal. In this *resonant* case, the ions have the highest kinetic energy when ejected through the magnetic field gradient towards the detector. By scanning the frequency of this rf-field the minimum ToF to the detector is determined which corresponds to the free cyclotron frequency of the trapped particle and yields the mass.

2.3. Precise Mass Determination of ^{208}Fr

For a Penning-trap mass measurement, a triplet of three resonances is required. First, the frequency of the reference mass has to be measured, then the ion of interest, and finally the reference mass for a second time. In order to take frequency drifts into account the reference-mass frequency is interpolated linearly to the time at which the wanted ion was measured. Two such triplets have been taken for ^{208}Fr with a 1200 ms excitation time and ^{133}Cs as reference mass. The ToF spectrum of one measurement is shown in fig. 2.4 [1].

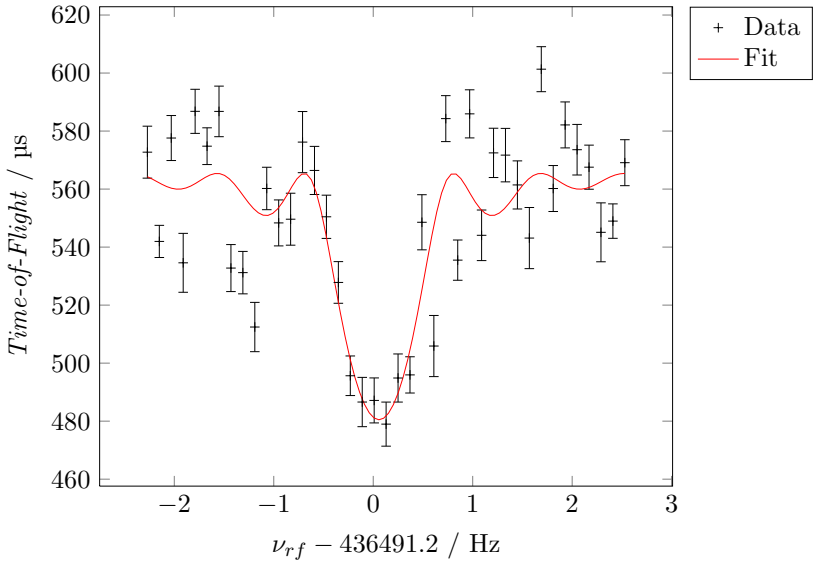

Figure 2.4.: The ToF spectrum of the ^{208}Fr measurement. In the centre the excitation frequency matches the cyclotron frequency, and the energy of the magnetron motion is converted into the modified cyclotron motion.

From eqn. (2.1) it follows that the mass m_x of the wanted nucleus can be determined through the ratio between the frequency of the reference ion and its own frequency $r = \omega_{ref}/\omega_x$ via

$$m_x = r(m_{ref} - m_e) + m_e \,. \tag{2.9}$$

Because singly-charged ions are measured, the mass of the electron has to be compensated. The mass of ^{208}Fr could be determined to

$$m(^{208}\mathrm{Fr}) = 207.997\,132\,7(72)\,\mathrm{u}\,. \tag{2.10}$$

[1] Preliminary results are part of the PhD thesis of Ch. Borgmann and have been measured during this Bachelor thesis.

Usually, not the mass but a quantity called *mass excess ME* is determined. It describes the binding energy of a nucleus assuming the same mass for a proton and a neutron. It is $ME = m - A\mathrm{u}$. The mass excess of ^{208}Fr is

$$ME(^{208}Fr) = -2670.8(67)\,\mathrm{keV}\,. \tag{2.11}$$

This value agrees well with the literature [6] but the error is almost an order of magnitude smaller than previous value of $ME(^{208}Fr_{pre}) = -2665(46)\,\mathrm{keV}$.

2.3.1. Reference Mass and Mass Uncertainty

The total uncertainty of the mass measurement is composed of the statistical and the systematic uncertainties of the frequency ratio δr and of the uncertainty of the reference mass δm_{ref}

$$\delta m_x = \sqrt{(m_{ref}\delta r)^2 + (r\delta m_{ref})^2}\,. \tag{2.12}$$

Eqn. (2.12) shows the dependency on the knowledge of the reference mass. For the exact formulation of δr the statistical error and furthermore different systematic errors have to be taken into account. Such, systematical errors are magnetic-field drifts, temperature fluctuations and a mass-dependent effect as investigated in [7]. Within this thesis the systematic uncertainty of the mass difference between the reference mass and the wanted mass will be brought to focus. In [7], it was found to be the following linear relation

$$\frac{u_m(r)}{r} = \frac{1.6 \times 10^{-10}}{\mathrm{u}}(m_x - m_{ref})\,. \tag{2.13}$$

The higher the mass difference, the higher the uncertainty of the final mass measurement. To this end, it is important to reduce the mass difference. Carbon clusters are the ideal candidate since they span a narrow net over the whole nuclear chart as shown in fig. 2.6.

2.4. ^{12}C as a Reference Mass

Using ^{12}C as reference mass, the maximum mass difference to a certain atom is at most 6 u and the systematic error of eqn. (2.13) decreases to a minimum. Another particular advantage is that it exhibits no internal uncertainty since the unified atomic mass unity is defined by 1/12th of a ^{12}C atom. Only the binding energy changes around a few eV [7] which is negligible compared to the uncertainty of 13 keV of ^{133}Cs which is commonly used as a reference for heavy masses [8]. Hence, the last term in eqn. (2.12) vanishes.
Carbon clusters $^{12}C_n$ can be obtained from the laser ion source at ISOLTRAP providing multiples of the mass 12 u with factors $n = 1$ until $n = 27$ [9] as shown in fig. 2.5. This makes it possible to provide suitable reference masses for ions with masses above 200 u where the error introduced by using ^{133}Cs as reference mass is no longer negligible. If carbon clusters $^{12}C_{17}$ had been used for the ^{208}Fr measurement the uncertainty of *ME* would be 3 % less and only 6.5 keV.

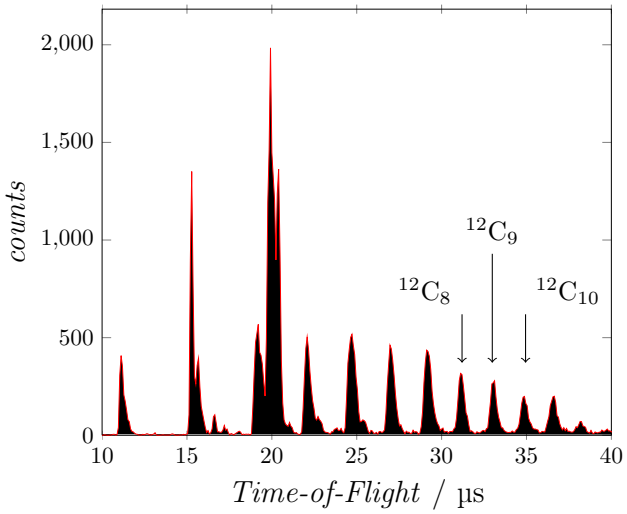

Figure 2.5.: Time-of-flight spectrum of carbon cluster at MCP1. Every peak represents a certain cluster species.

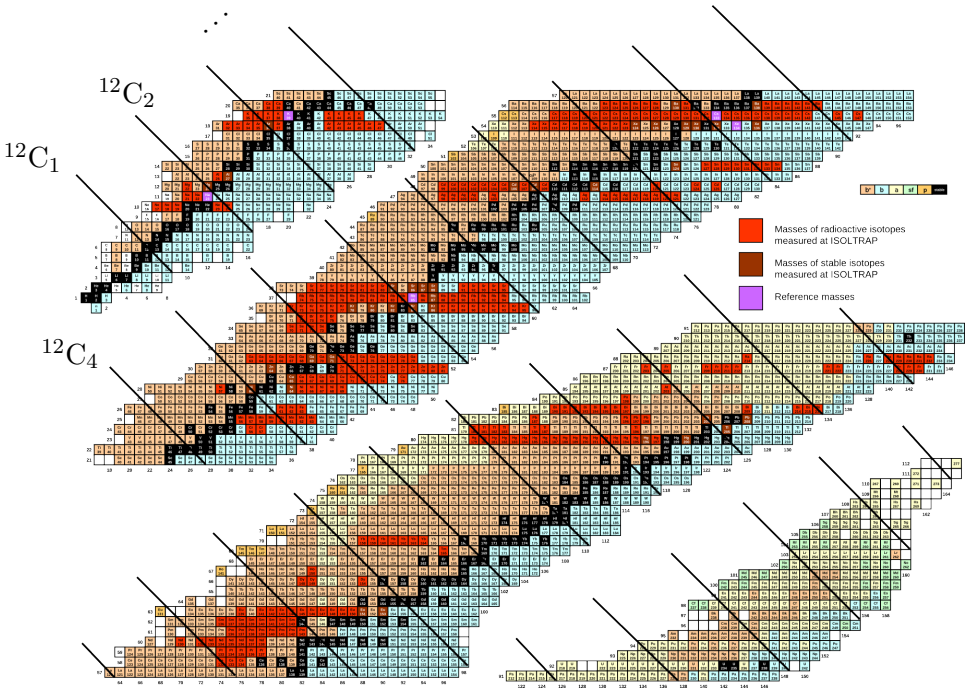

Figure 2.6.: Nuclide chart of measured nuclei together with common reference masses. The black lines display the masses covered by Carbon clusters [10].

3. The Laser Ion Source at ISOLTRAP

The laser ion source at ISOLTRAP not only provides carbon clusters but also the palladium isotopes ^{102,106,108,110}Pd. Since these spread over a smaller mass range, they are favoured to optimise the ion transport from the laser ion source to the detector. Within this thesis, ^{108}Pd was used primarily.
In the following, the principles of laser ablation and the setup of the laser ion source are described. Then, the laser-beam setup and the implementation of a telescope are presented. Finally, the count-rate fluctuations and the energy selection of ions via a pulsed cavity are discussed.
The number of ions obtained from the laser ion source varies around a certain mean value erratically from very high count rates to zero. On the one hand, the high count rate leads to an overpopulation of the Penning trap where space charge effects disturb the rf-excitation. On the other hand, the zero counts extend the required time for a measurement which increases the statistical error. There had been two approaches to reduce these fluctuations:

1) Exchange of the formation chamber and the extraction electrode with a Pierce-geometry which is expected to reduce unknown parameters during the creation of the ions and provide better starting conditions. The appropriate geometry was found by simulations, see chapter 4.

2) Implementation of a telescope into the laser beam line. Thereby, the beam width at the focal point can be decreased which leads to a higher power density at the target. This increases the yield for the same laser power. Thus, lower laser energies yield more constant count rates. Furthermore, the spatial distribution of the extracted ion pulse would be more narrow which is advantageous for the transport, see the results in section 3.3.

3.1. Principles of Laser Ablation

A laser hitting a surface with sufficient energy can detach atoms and a plume of material is created over the surface. Depending on the length and the energy of the pulse, different effects cause the particles to exhibit complicated energy and spatial distributions.
For low laser energies, atoms will be evaporated which will be weakly charged or even neutral. This plume would have a Maxwellian velocity distribution since it is a free gas. For higher laser energies, in addition a shock wave component will be superimposed because of the impact on the target, and a plasma will be created as shown in fig. 3.1. Charge exchange will appear, causes particles to interact and different sizes of clusters

can be formed in this process [11]. The depth to which the material is removed also depends on the energy but in general only a few atomic layers are ablated. The Gaussian beam profile of the laser leads to a Gaussian spatial distribution of the ablated ions.

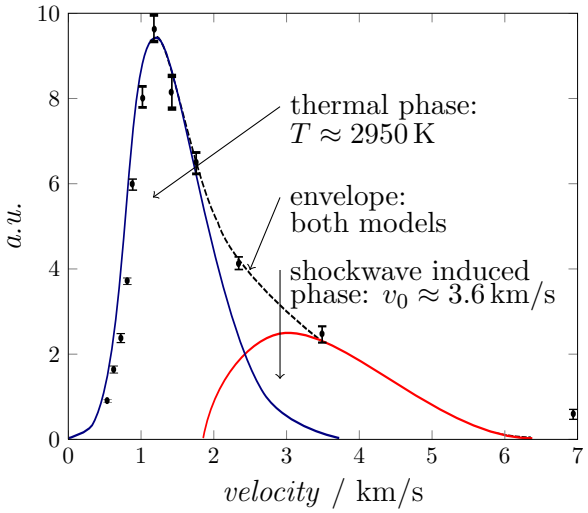

Figure 3.1.: Velocity distribution of laser-ablated ions. The total distribution is a superposition of a Maxwellian distribution and a ballistic shock wave distribution [11].

3.2. The Setup of the Laser Ion Source and the Laser Beam Line

A nanosecond, frequency-doubled 532 nm Nd:YAG laser (*Polaris III*) aims perpendicularly at a partitioned target which can be rotated to choose a certain target area. The target consists of a glassy carbon pellet (SIGRADUR® by *HTW*) for the cluster production and a high-purity metallic palladium foil (*Alfa Aesar*). The ablated ions start from a potential of 3.1 kV applied to formation chamber and pellet. Then, they are accelerated by the potential difference between formation chamber and extraction electrode towards an einzel lens and a set of steerers to prepare the beam for the following beam line. The laser ion source is shown in fig. 3.2 and the laser beam set-up in fig. 3.3. Behind the steerers, the ion beam is guided into the main beam line by a 90 °-quadrupole deflector (not shown). However, a well-defined ion beam cannot be extracted. The opening of the extraction electrode is small compared to the exit of the formation chamber which causes many ions to hit the extraction electrode, which constitutes on reason for the low beam quality.

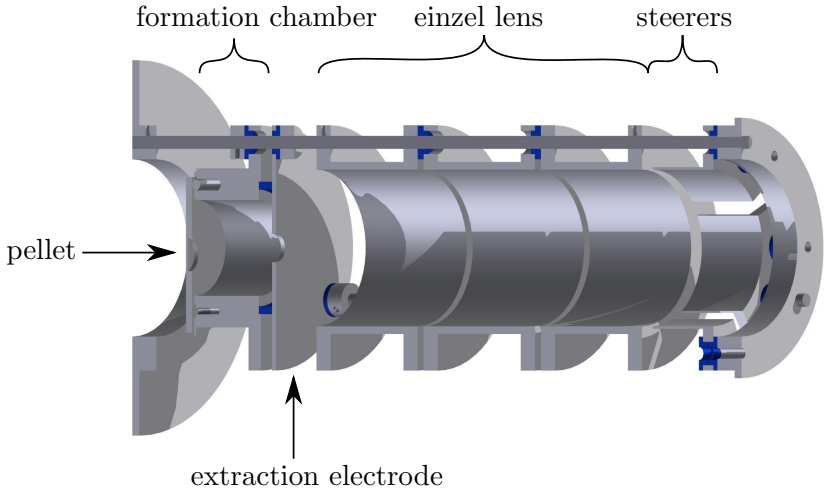

Figure 3.2.: Layout of the former laser ion source with ion-optical elements.

3.3. Implementation of a Telescope into the Laser Beam Line

The properties of the ablated ions depend strongly on the power density which increases for a smaller laser beam. A smaller focal point would yield the following advantages:

- It is expected to reduce the width of the Gaussian profile of the laser and thereby the spatial distribution of the ablated ions. The beam would be more narrow which makes it easier to guide.
- The production of ions depends directly on the energy density (fluence) at the target [12]. Since fluence is power per area which the laser hits, it can be increased by a smaller focal point. Measurements have shown that for low laser powers like at ISOLTRAP ($\approx 20\,\mathrm{MW/cm^2}$), the yield increases strongly with the fluence which is also expected to stabilise the count rate.

To achieve a smaller focal point, a telescope (two lenses with focal length 2.5 cm and 10 cm) has been installed between the last two mirrors as shown in fig. 3.3. This increases the laser width in front of the last lens and thereby a stronger focus at the target can be achieved. The laser width was measured with and without the telescope with the knife-edge method as performed also in [13] for several distances to the lens. Hereby, a sharp object is slid into the laser beam stepwise while the transmitted power is measured. The transversal laser-power profile follows the function

$$P_{tot} = \frac{P_{tot}}{2}\left(1 + \mathrm{erf}\left(\frac{\sqrt{2}(x - x_0)}{w_x}\right)\right), \tag{3.1}$$

where P_{tot} is the total power of the beam, x_0 the position of the edge and w_x the $1/e^2$-width of the laser beam. This has been done for several distances around the focal point. The

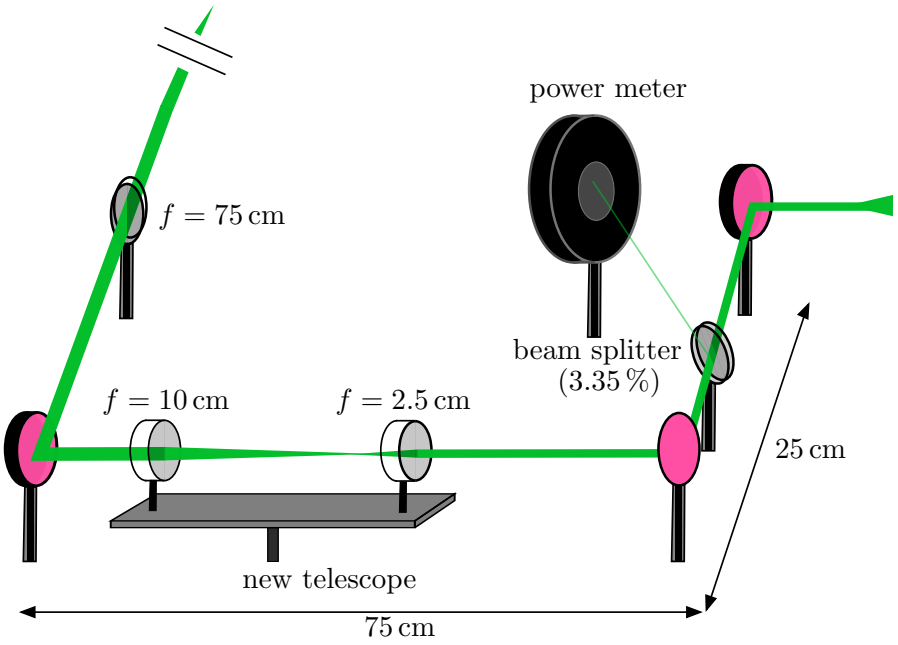

Figure 3.3.: The present laser-beam-line setup. The new telescope is located between the two last mirrors which are used to align the beam through the ion source. On the right, a beam splitter couples out 3.35 % of the laser power which can be monitored by a power meter. On the left, the beam enters the ion beam line after the $f = 75\,\mathrm{cm}$ lens where it hits the pellet (not shown).

measurement in a distance of 55 cm to the lens is shown in fig. 3.4 on the left as an example.
In order to determine the focal width w_0, the widths from the different distances have been fitted to the theoretical longitudinal shape of Gaussian laser beam

$$w(z) = w_0 \sqrt{1 + \left(\frac{z - z_0}{z_R}\right)^2}, \tag{3.2}$$

as shown fig. 3.4 on the right. The focal distance is z_0 and z_R is a scaling factor. For the minimum width, the values of tab. 3.1 have been found. These values differ

	w_0 / mm (no telescope)	w_0 / mm (telescope)
vertical	0.845(15)	0.344(16)
horizontal	0.939(14)	0.192(15)

Table 3.1.: Results for the laser widths with and without the telescope.

from the ones of [13] as they are about 30 % smaller, which is due to modifications of the setup. Since the shape of the laser beam is elliptical, its area at the focal

point is at least $A_{beam} = \pi \cdot w_0^{hor} w_0^{ver}$. The resulting area is 2.493(45) mm^2 without and 0.208(48) mm^2 with the telescope. This means about 12 % can be gained in power density.

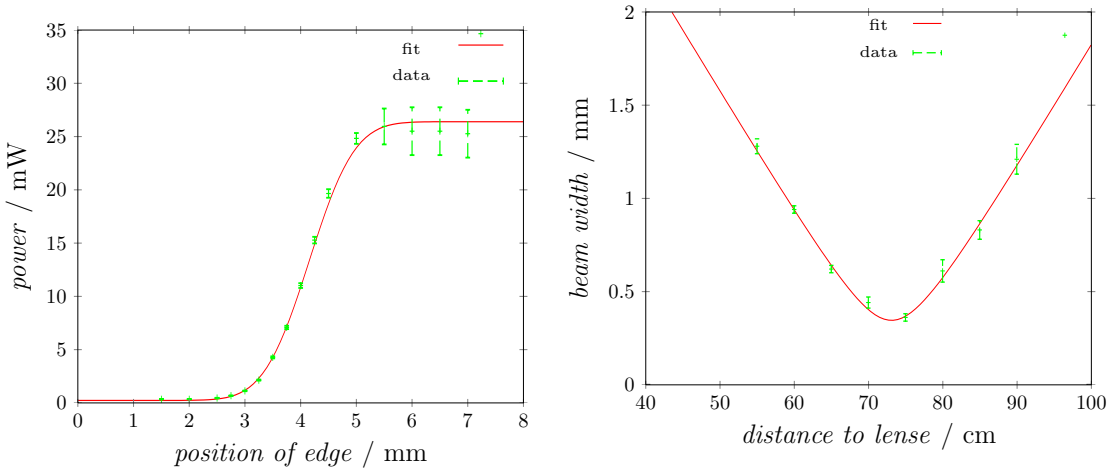

Figure 3.4.: Left: Data from the knife-edge measurement with the telescope. Right: Vertical width profile of the laser beam. The width of the beam is shown at different distances to the lens. The red lines are fits with the theoretical formulae given in eqn. (3.1) and eqn. (3.2).

3.4. Measurements of the Count-Rate Fluctuations

Fluctuations appear for all elements obtained from the laser ion source. The count rate of ^{108}Pd has been measured for 200 laser pulses after the ejection from the preparation trap on MCP2 (compare fig. 2.2). This was repeated for different laser powers. Part of a measurement is shown in fig. 3.5. The power was regulated by the voltage of the laser flash lamp (PFN). In fig. 3.6, the count rate measurements with the telescope and without are shown, respectively.

In general, the ablation process starts at about PFN = 80 % and a value higher than 83 % is needed to work in a stable region. The fluctuations seem to stay constant for different PFN values which might be partly caused by saturation of the MCP. A typical value for measurements is 86 %. With telescope, the shape of the yield curve is steeper due to the energy density increase. The energy density now grows per PFN with a factor of 8 faster than without the telescope.

Unfortunately, the fluctuations did not vanish. But an interesting feature did occur: for PFN values from 83 % to 85 %, which correspond to a fluence of about 11 MW/cm^2 to 14 MW/cm^2 a plateau in the the count rate became visible. The dashed line in fig. 3.6 describes the expected developing. This plateau cannot be explained by the charge compensation of the ions as studied in [11]. Hereby only dual charged ions exchange electrons with neutral atoms whereby the yield reduces. Until now, the origin of the

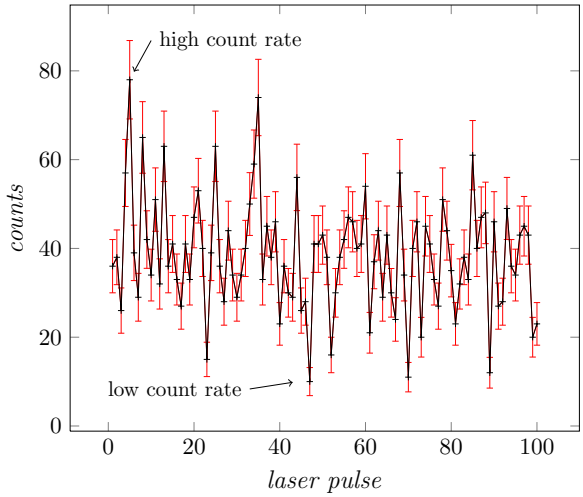

Figure 3.5.: Count rate of ^{108}Pd over 100 laser pulses at MCP2. For details see text.

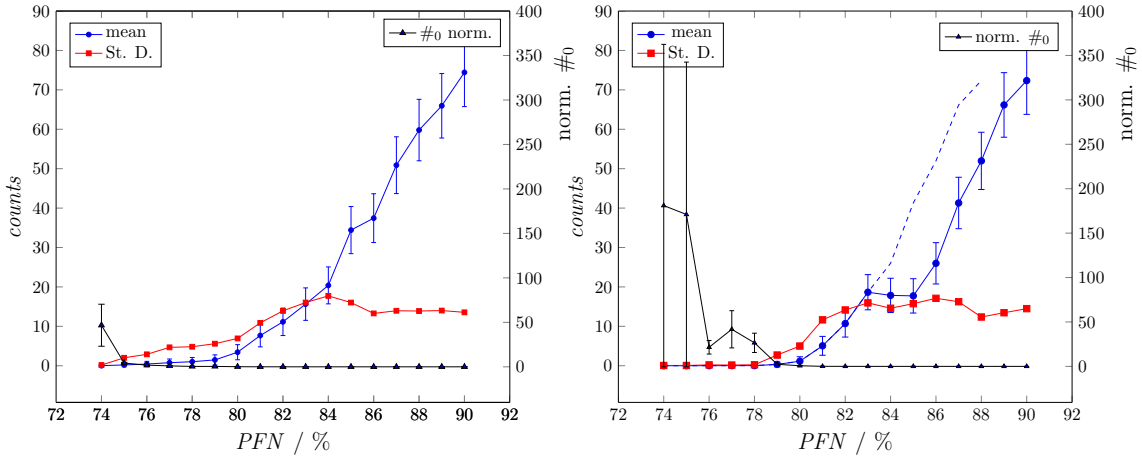

Figure 3.6.: Count rate of the laser ion source for different laser energies with (right) and without (left) telescope. Mean value and standard deviation (left scale) as well as the number of zero counts ($\#_0$) normalised to the total number of ions (right scale) are shown.

plateau could not be understood and has be investigated further.

3.5. Energy Selection by the Length of the Switched-Cavity Pulse

In order to capture the ions in the preparation Penning trap, a switched cavity is used to reduce the energy of the ions relative to the trapping potentials. Pulse length and timing of the cavity together with suitable injection into the trap can be used to select

narrow energy ranges of the incoming ion cloud to minimise fluctuations. The standard deviation and the number of zero counts has been evaluated for pulse lengths between 2 µs and 3 µs in combination with different settings for the injection. For a pulse length of 3 µs and an energy of the ions of 50 eV as compared to the trapping potential of 100 eV, the standard deviation stays constant around 5 counts as shown in fig. 3.7, and yields a favourable configuration.

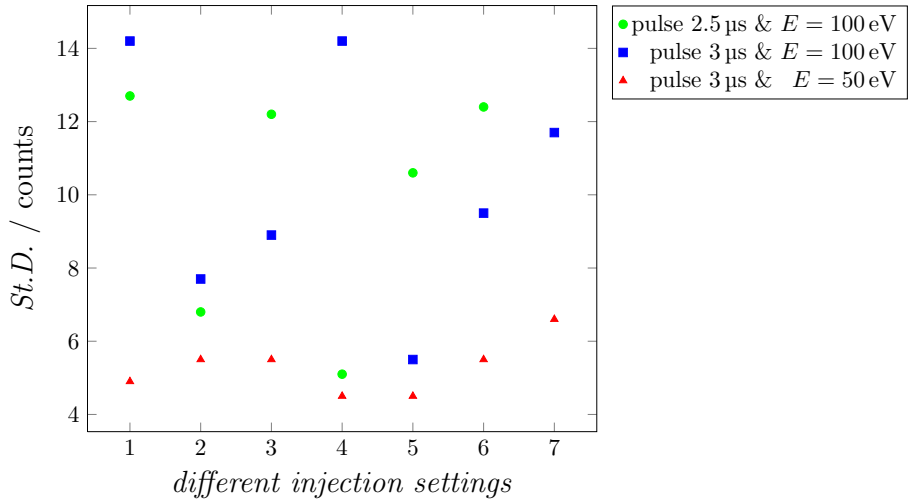

Figure 3.7.: Standard deviation (St.D.) of ion counts at MCP2, trapping at different injection pulse and cavity (SW-) settings (see tab. 3.2).

SW− pulse / µs / µs	SW− delay / µs / µs	LT inj. pulse / µs / µs	LT inj. delay / µs / µs	St. D. / counts	norm. $\#_0$ counts
		$E = 100\,\mathrm{eV}$			
2.5	26.7	5	45	12.7	0.01
2.5	26.7	5	50	6.8	0.10
2.5	26.7	10	45	12.2	0.01
2.5	26.7	10	50	5.1	0.12
2.5	26.7	40	36	10.6	0.04
2.5	26.7	40	46	12.4	0.01
3.0	26.0	5	46	14.2	0.00
3.0	26.0	5	50	7.7	0.09
3.0	26.0	10	43	8.9	0.04
3.0	26.0	10	45	14.2	0.01
3.0	26.0	10	51	5.5	0.17
3.0	26.0	40	36	9.5	0.04
3.0	26.0	40	46	11.7	0.01
		$E = 50\,\mathrm{eV}$			
3.0	26.5	5	45	4.9	0.11
3.0	26.5	5	50	5.5	0.20
3.0	26.5	10	45	4.5	0.06
3.0	26.5	10	50	4.5	0.20
3.0	26.5	40	36	5.5	0.12
3.0	26.5	40	46	6.6	0.08

Table 3.2.: Injection settings of the energy matching with standard deviation (St. D.) and the normalised number of zero counts.

4. Design of a new Extraction Electrode

The transfer of ions through an apparatus, which is dedicated to investigate their properties, plays an important role. From a laser ion source the ions start with their spatial and kinetic energy distribution widely spread. This makes it difficult to transport all particles created and at the same time form a well-defined beam. It is desired to create a parallel beam to facilitate transport and beam manipulation. The extraction electrodes, which are located at the creation point of the ions, define the initial potential and are therefore crucial for the beam quality and initial conditions. In this chapter, the derivation of the Pierce geometry will be discussed together with the simulations that led to the final design. New electrodes have been manufactured according to the technical drawings of section 4.3.

4.1. Derivation of the Pierce-Geometry Extraction Electrode

The ideal shape of the extraction electrodes to create a parallel beam can be derived from the maximum current density which is possible for a space-charge dominated ion source [1]. This particular geometry is called a Pierce geometry. In the next two sections the *Child law*, which states the maximum current density from a space charge dominated injector will be outlined, and from that the Pierce geometry will be derived for the one-dimensional case. The three-dimensional solution has to be found numerically which would go beyond the scope of this work.

4.1.1. Child Law

The most simple way to describe an extraction electrode is an infinitely extended plate on a negative potential Φ_0. It accelerates positively charged ions, which are provided by a grounded electrode, with likewise infinite extension and is located at distance d to the latter. The flux of ions is a priori unlimited. This configuration is shown in fig. 4.1. Consider ions entering the space between the electrodes at a certain time. Then, the electric field is only generated by the potential at the plates. But the more ions enter the space from the source electrode, the weaker becomes the field until it finally vanishes at the surface of the source. At this point, the current density has reached its maximum. In the one-dimensional case, the potential can be found as [14, 15]

$$\Phi(z) = \Phi_0 \left(z/d\right)^{\frac{4}{3}} \ . \tag{4.1}$$

Here, the ions are accelerated in z-direction and the field is equal to zero at the origin as required.

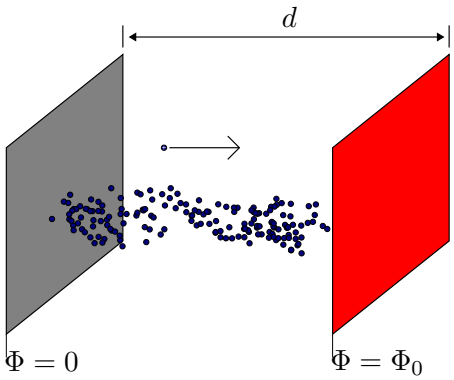

Figure 4.1.: Configuration of the electrode geometry of the Child law.

4.1.2. The Shape of the Pierce Electrode

The aim for the laser ion source is to extract the ions in a beam as narrow as possible and ideally without any divergence. These requirements are satisfied by the Pierce geometry [1], which can be derived from the potential variation obtained by the Child law.
The starting point is to create a field which surrounds a space-charge dominated beam with a certain radius. This field should provide the same conditions like as the beam was infinitely extended. Under these conditions, the Child law holds and the variation of the potential along the beam is as stated in eqn. 4.1. The field has to be provided by the electrodes and therefore their shape can be determined from it.
It has to be noted that these calculations were always done for ions which leave the anode perfectly parallel and thus the Pierce geometry *preserves* the initial beam conditions. To simplify calculations, only one point on the edge of the beam is considered with the following boundary conditions:

(1) The potential has to be described by eqn. (4.1).

(2) Since there cannot be a transversal force at the edge without changing the shape of the beam, it is required that $\partial\Phi/\partial x = 0$.

The Laplace equation has to be solved for these conditions, which can be done by means of the complex variable $u = x + iz$. Every analytical function of $f(u)$ is a solution to the Laplace equation which can be shown by using the chain rule. Thereby

$$\Phi = \Phi_0 \mathrm{Re}\left(\frac{z+ix}{d}\right)^{\frac{4}{3}} \tag{4.2}$$

is a possible solution which satisfies the two conditions.
In order to realise this field, the electrodes must be shaped like equipotential lines. The field can be imaged to the geometry by introducing polar coordinates

$$x = r\sin(\theta) \quad \text{and} \quad z = r\cos(\theta) \tag{4.3}$$

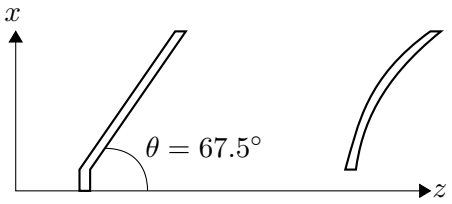

Figure 4.2.: Original geometry for the Pierce solution. On the left side, the source electrode where the ions enter the configuration along the z-axis. On the right, the bended extraction electrode.

and by using the Euler relation $e^{i\theta} = \cos(\theta) + i\sin(\theta)$. Thus, the potential becomes

$$\Phi = \Phi_0 \mathrm{Re}\left(\frac{r}{d}e^{i\theta}\right)^{\frac{4}{3}} = \Phi_0 \left(\frac{r}{d}\right)^{\frac{4}{3}} \mathrm{Re}\left(e^{\frac{4\theta}{3}}\right) . \tag{4.4}$$

For the source electrode $\Phi = 0$ holds, which yields the condition $4\theta/3 = \pi/2$. In other words, the source electrode must be shaped like a plane with a 67.5° angle to the beam axis. The second electrode is slightly more complicated. Its shape follows

$$\left(\frac{r}{d}\right)^{\frac{4}{3}} \cos\left(\frac{4\theta}{3}\right) = 1 , \tag{4.5}$$

which is a curved electrode. The configuration is shown in fig. 4.2.

4.2. Simulations of Ion Motion in Different Geometries

The starting conditions of the laser ablated ions at the laser ion source deviate from the ones in the Pierce solution. To take these deviations into account, simulations have been performed to find an optimum shape and configuration of the future electrodes[1]. A configuration as in fig. 4.3 has been investigated. The curved shape of the extraction electrode was simplified to a cone in order to facilitate the manufacturing process.
The parameters, which have been analysed, were (1) the number of particles which were lost by hitting a surface, (2) the divergence and (3) the emittance of the ion beam. The number of lost particles has been the most crucial parameter since the number of zero counts should be reduced as much as possible. The simulations have been performed with the software SIMION® and where divided in three steps.

Step 1 The three distances z_{12}, l_2 and R_2 shown in fig. 4.3 have been varied while the angle of the source electrode has been set to the Pierce angle. While one parameter was fixed, the other two were varied.

Step 2 For the optimum configuration of step 1, the radii r_1 and r_2 of the holes in the electrodes have been varied.

[1]The simulations are part of the PhD thesis of V. Manea.

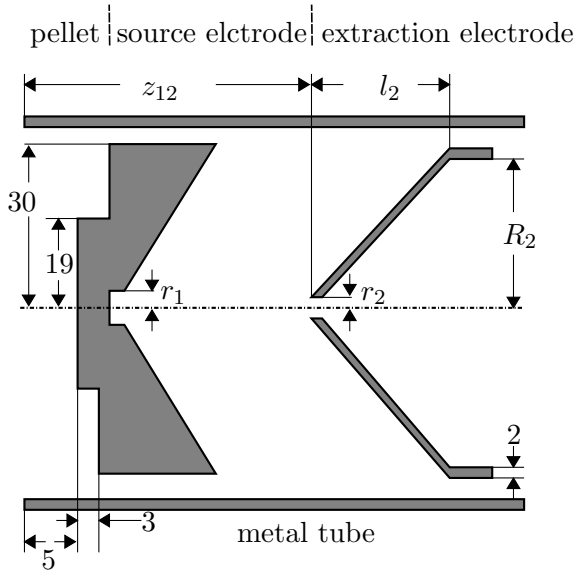

Figure 4.3.: Setup of the simulations. On the left, the pellet with the source electrode combined to one part and on the right the extraction electrode are shown. The potential difference had been set to 4.66 keV which corresponds to the latest settings in the experiment.

Step 3 With the resulting geometry, the previously fixed angle of the source electrode has been varied.

4.2.1. Starting Conditions of the Ion Population and Results

A total of 324 ions with Maxwellian kinetic-energy distribution have been simulated. For every geometrical configuration, two types of populations were used, one with an isotropic Maxwellian distribution and one with a 3000 m/s boosted longitudinal velocity to take the ballistic velocity component into account (see section 3.1). For the spatial distribution, a Gaussian has been chosen to match the energy profile of the laser. The centre of the distribution was located 1 mm in front of the pellet and spread over 1.8 mm in all spatial directions. Starting values for the two inner radii of the electrodes of $r_1 = 3.25\,\text{mm}$ and $r_2 = 4\,\text{mm}$ were used for the first set of simulations.

Step 1

The influence of the radius of the extraction electrode R_2 on the number of lost particles and the other parameters is almost negligible. A value of $R_2 = 28\,\text{mm}$ has been chosen, since smaller values in combination with a larger inter-electrode distance lead to a greater loss of particles because of the decreasing guiding field.
The effect of the variation of the distance between the two electrode z_{12} and the length of the second electrode l_2 on the number of lost particles as well as the beam divergence are

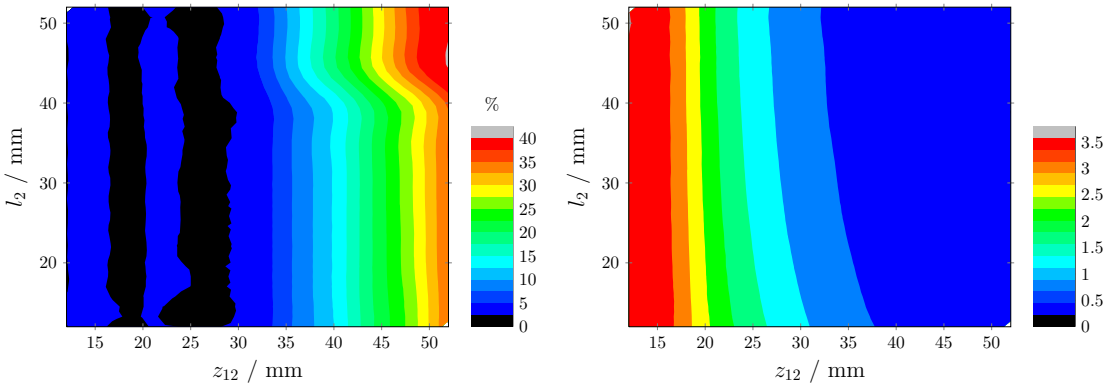

Figure 4.4.: Results of step 1 in the simulations. Left: Percentage of lost particles for different distances between the electrodes z_{12} and lengths of the second electrode l_2. Right: Relative divergence with respect to the minimum (9.74 mrad) of the ion beam after the second electrode.

shown in fig. 4.4. For the distance z_{12} two minima are found with respect to the number of lost particles. The value $z_{12} = 25\,\text{mm}$ was chosen to minimise the divergence. For this configuration, the distance between the electrodes l_2 influences the parameters only slightly, which might be explained by the large potential difference over which the ions are accelerated. Considering geometrical constraints, the value has been set to $l_2 = 30\,\text{mm}$.

Step 2

First, the beam quality increases for a larger slit r_1 until it reaches a minimum as well as the number of lost particles, which equals zero for slits larger than a radius of 1 mm. Since the laser beam has a certain diameter, the slit was set to $r_1 = 4\,\text{mm}$, taking uncertainties in the alignment into account. The extraction slit shows very similar properties and the same reasons yield $r_2 = 3\,\text{mm}$ as a good compromise.

Step 3

In the last step, the angle of the source electrode was varied around the Pierce angle. An angle of 58°, which is smaller than the Pierce-angle, was found to provide better beam quality through stronger focus. This is shown in fig. 4.5 and can be explained by the fact that the Pierce angle was calculated for a beam without divergence. Again, the number of lost particles is negligible.

4.3. Technical Drawings of the Final Geometry

According to the final geometry of section 4.2 technical drawings were made with $R_2 = 28\,\text{mm}$, $z_{12} = 25\,\text{mm}$, $l_2 = 30\,\text{mm}$, $r_1 = 4\,\text{mm}$, $r_2 = 3\,\text{mm}$ and an angle of 58° for the extraction electrode. Both electrodes were manufactured from non-magnetic, stainless steel and are shown in fig. 4.6 (drawing and picture of the source electrode) and

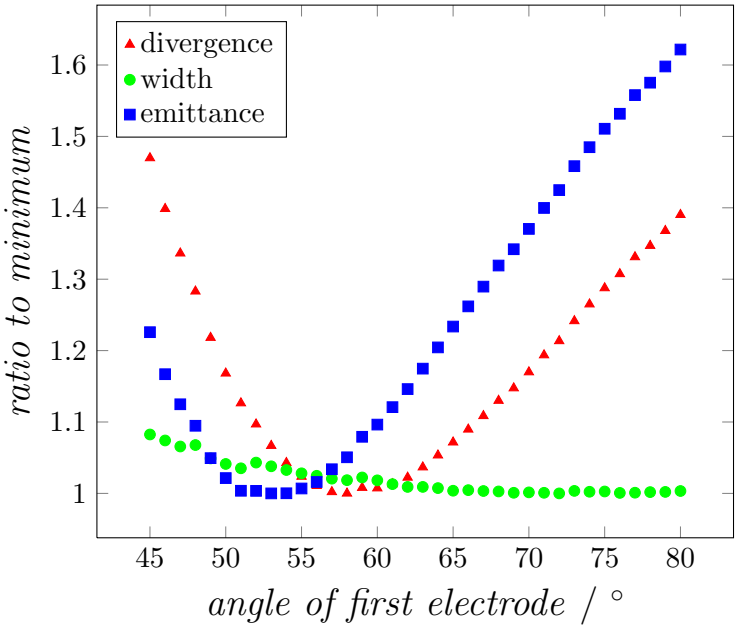

Figure 4.5.: Results of step 3 of the simulations. The angle of the source electrode is varied. At an angle of 58° all parameters have all low values.

in fig. 4.7 (drawing and picture of the extraction electrode). The commissioning of the modified laser ion source geometry could not be performed within the scope of this thesis due to time constraints.

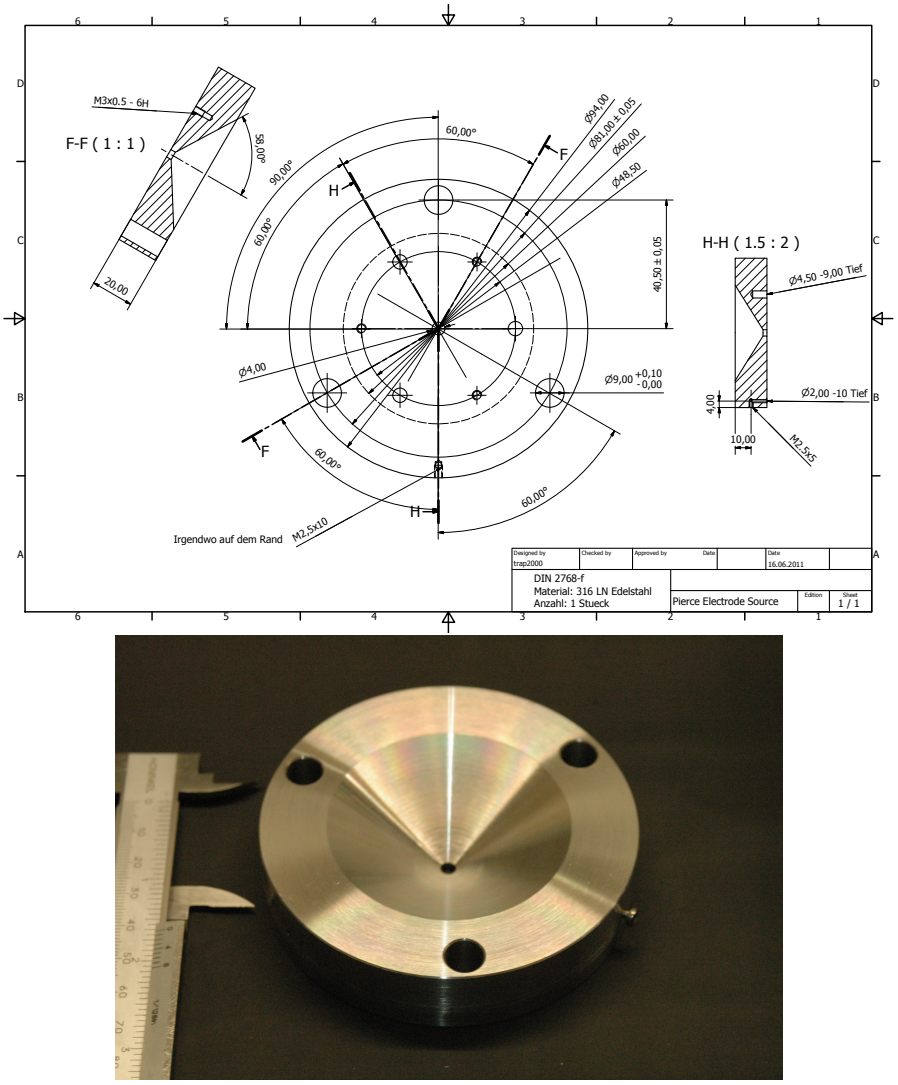

Figure 4.6.: Top: Technical drawing of the new source electrode which replaces the formation chamber. Bottom: Picture of the new source electrode.

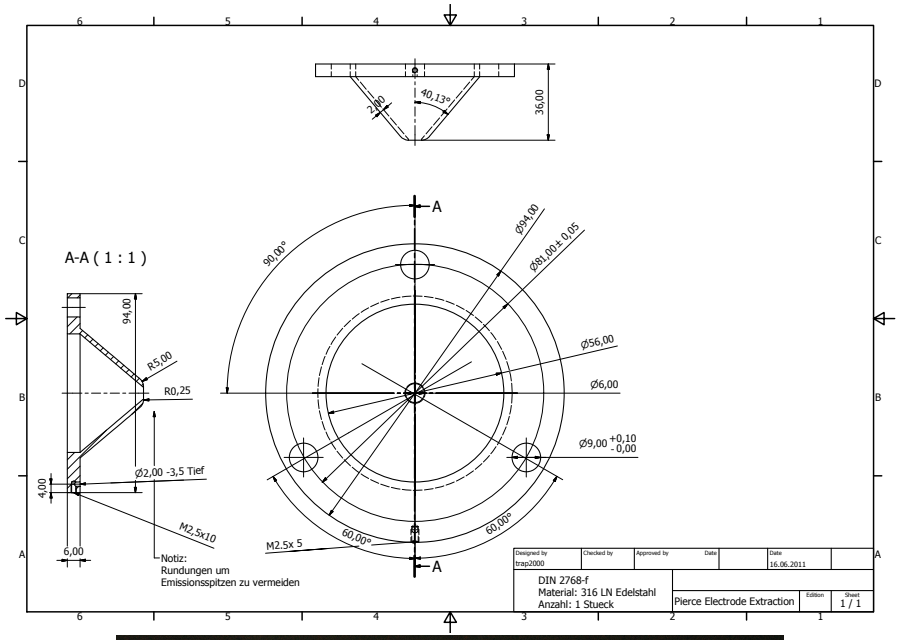

Figure 4.7.: Top: Technical drawing of the new extraction electrode. Bottom: Picture of the new extraction electrode.

5. Conclusion

Within the scope of this work, detailed technical drawings of the laser ions source at ISOLTRAP had to be produced, which are shown in the appendix. The setup had to be modified, in order to obtain a stable and high-quality ion beam. In addition, it had been participated in three on-line runs, from which preliminary results have been presented.
Decreasing the fluctuations in the output rate of the laser ion source at ISOLTRAP has been the main goal of this work. Hence, three different approaches have been made. First, a new extraction electrode geometry had been designed and manufactured. Starting from the ideal solution for a parallel electron beam, the shape was derived by simulating the ion motion for different geometries. Mainly, the number of particles which were lost at surfaces and the divergence of the out-coming beam were the parameters which have been optimised. Furthermore, the power density at the target had been increased by the implementation of a telescope. This increases the count rate which is expected to reduce the fluctuations. The aim of less fluctuations could not be achieved but it is now possible to adjust the power density by the focus of the telescope. At last, energy ranges of the trapped ion cloud were selected to minimise the energy distribution of the ions entering the preparation trap. New configurations for the pulse length and the injection delay for the lower trap have been found.
In summary, the count rate fluctuations from the laser ion source has been investigated in detail. Further steps are required to understand and to control the output of the laser ion source. At first, the source and extraction electrode have to be implemented and commissioned. Afterwards, the count rate should be investigated at a detector as close to the ion source as possible to minimise influences from the ion transport through the beam line. Ideally, a MCP detector should be available in front or directly behind the 90°-deflector rods. As a first test, the count rate should be optimised with respect to the potential applied to the source and extraction electrode. Subsequently, the ion beam transport through the ion-optical elements of the beam line has to be tuned. With these modifications, it is expected to realise reproducible carbon cluster rates for the use of reference masses with the laser ion source at ISOLTRAP.

A. Technical Drawings and Element Assignment

A.1. Complete Laser Ion Source

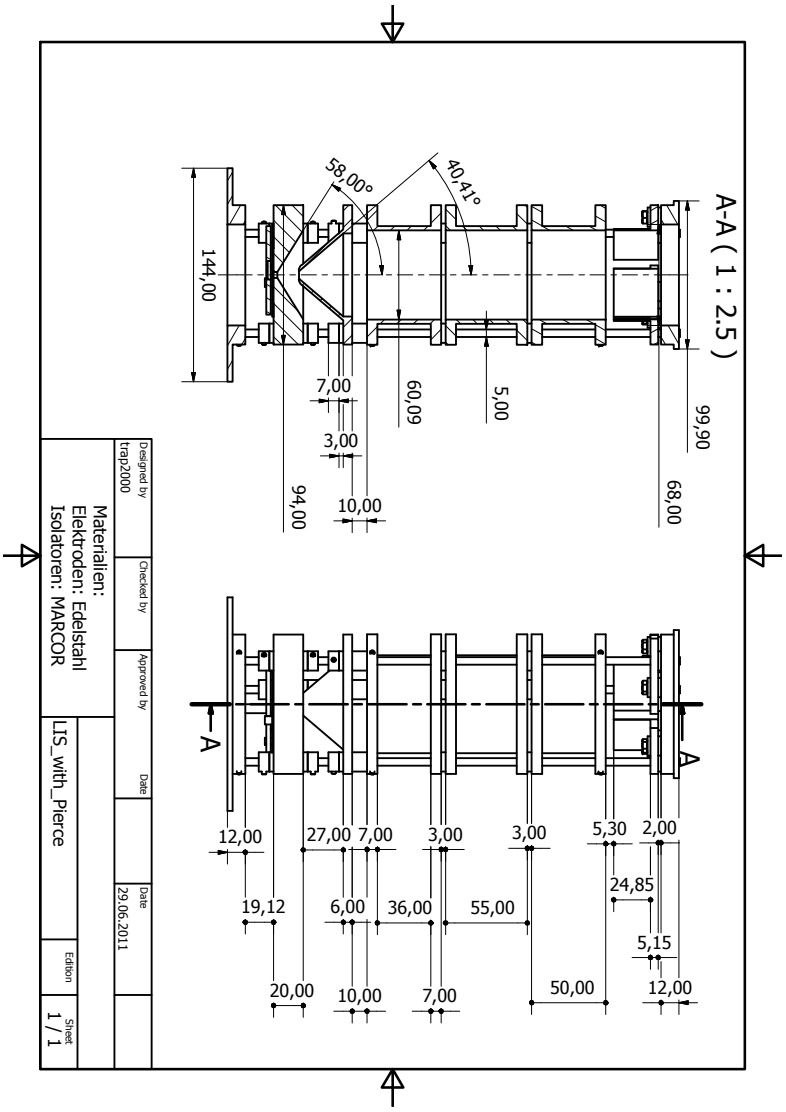

Figure A.1.: The dimensions main of the laser ion source with new electrodes.

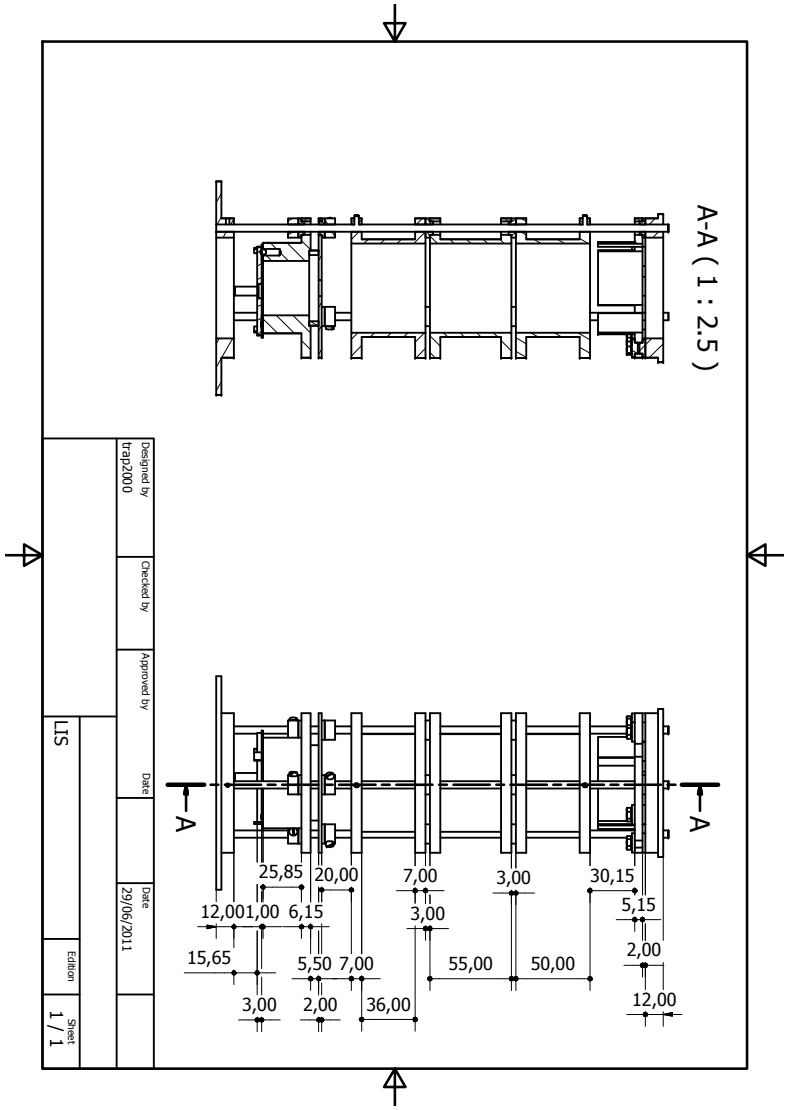

Figure A.2.: The main dimensions of the laser ion source with the formation chamber geometry.

A.2. Insulaters and Mounting Rings

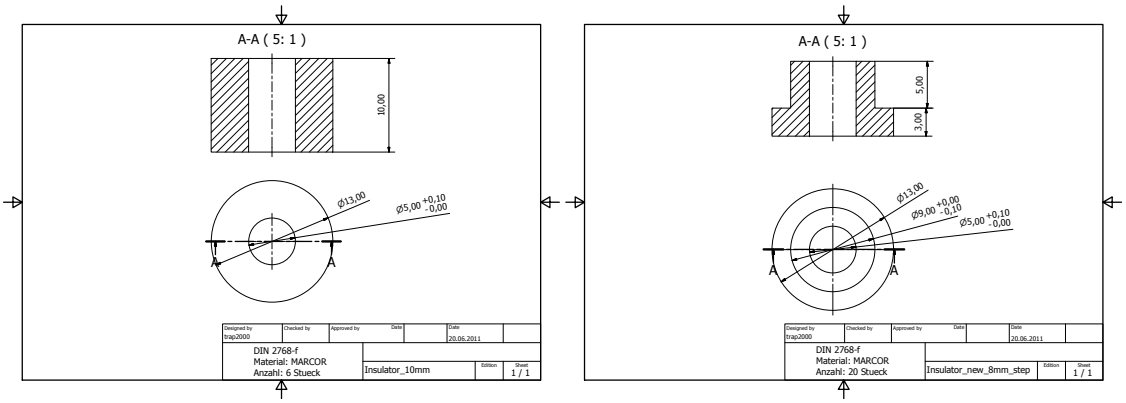

Figure A.3.: Technical drawings of the new insulaters.

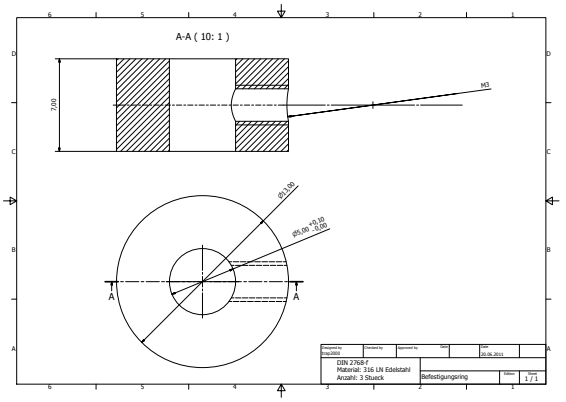

Figure A.4.: Technichal drawing of the mounting rings.

A.3. Assignment of Ion Optical Elements at the Laser Ion Source

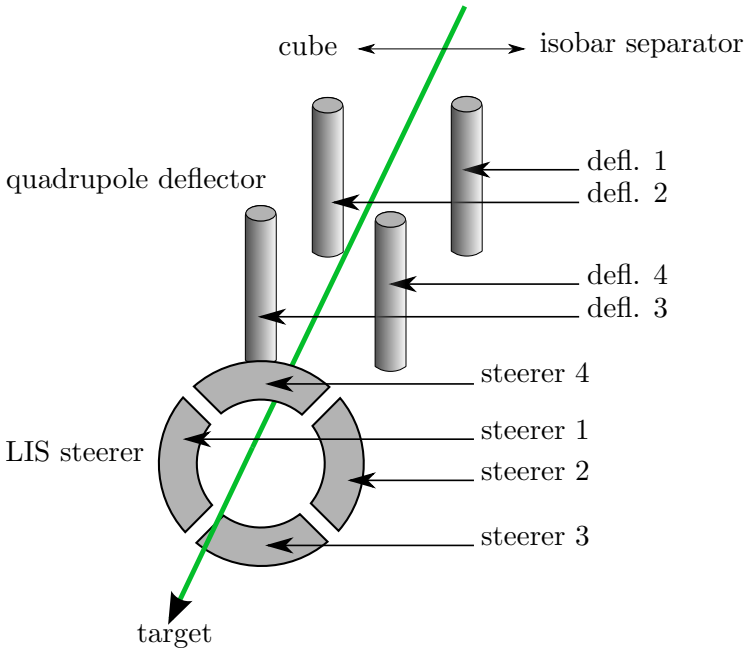

Figure A.5.: Ion-optical elements at the laser ion source. From the extraction electrode the ions pass the LIS steerer and are deflected to the left by the quadrupole deflector afterwards.

Bibliography

[1] J. R. Pierce, *J. Appl. Phys.* **11**(8), 548 (1940).

[2] C. Smorra, et al., *J. Phys. B.* **42**, 154028 (2009).

[3] K. Blaum, *Phys. Rep.* **425**, 1 (2006).

[4] T. J. Giles, et al., *Nucl. Instr. Meth. B* **204**, 497 (2003), 14th International Conference on Electromagnetic Isotope Separators and Techniques Related to their Applications.

[5] M. König, *Präzisionsmassenbestimmung instabiler Cäsium- und Bariumisotopein einer Penningfalle und Untersuchungen der Ionenbewegung bei azimutaler Quadrupolanregung*, Ph.D. thesis, Johannes Gutenberg-Universität Mainz (1995).

[6] A. H. Wapstra, G. Audi, C. Thibault, *Nuclear Physics A* **729**(1), 129 (2003), The 2003 NUBASE and Atomic Mass Evaluations.

[7] A. Kellerbauer, et al., *Eur. Phys. J. D* **22**, 53 (2003).

[8] D. Beck, et al., *Eur. J. Phys. A.* **8**, 307 (2000).

[9] K. Blaum, *Eur. J. Phys. A.* **15**, 245 (2002).

[10] Courtesy of K. Blaum .

[11] J. Maul, *Ortsaufgelöster Nachweis von Elementspuren mittels Laserablation und Resonanzionisations-Massenspektrometrie und Untersuchungen zur Laserablations-Dynamik*, Ph.D. thesis, Universität Mainz (2004).

[12] S. Amoruso, M. Armenante, V. Berardi, R. Bruzzese, N. Spinelli, *Appl. Phys. A* **65**, 265 (1997).

[13] D. Fink, 'The ISOLTRAP Laser-Ablation Ion Source and Q-Value Determination of the ^{110}Pd Double Beta Decay', Master's thesis, Johannes Gutenberg-Universität Mainz (2010).

[14] C. D. Child, *Phys. Rev. (Series I)* **32**(5), 492 (1911).

[15] S. Humphries, *Charged Particle Beams*. John Wiley & Sons (1990), accessed electonic version: http://www.scribd.com/doc/19234267/Charged-Particle-Beams-S-Humphries.

Danksagung

Mein Dank gebührt *Prof. Dr. Klaus Blaum* – für die Erfüllung des Traums einmal das CERN zu sehen und für das herzliche und unkomplizierte Willkommen vom ersten Kontakt an.

Dr. Susanne Kreim gilt mein aufrichtiger Dank für die großartige Betreuung vor Ort und vor allem in der Endphase mit so viel Kompetenz und Herzlichkeit. Danke für das Vertrauen vom ersten Moment an. Durch dich ist das hier erst möglich geworden und ich hoffe, dass diese besondere Erfahrung weiterhin für andere möglich sein wird.

Mulţumesk to *Vladimir Manea* for helping a lot in different parts during this work.

Danke *Kim Kreim* für die Hilfe bei der Laserjustage und für das Teleskop.

Danke *Robert Wolf* für die Ratschläge in letzter Minute bezüglich der Fertigung der Elektroden.

Christopher Borgmann danke ich für ein Dach über dem Kopf.

I would like to thank all the people who have been at ISOLTRAP during my short visit for the warm atmosphere at the platform. These are *Marco Rosenbusch, Christine Böhm, Martin Breitenfeld, Sarah Naimi, David Lunney, Thomas Cocolios, Magdalena Kowalska, Frank Wienholtz, Juliane Stanja, Lauriane Fouche, Burcu Cakirli, Gerrit Marx, Alexander Herlert, Frank Herfurth* and the ones above.

Zu allerletzt und vorallem danke ich meinen Eltern für alles. Ohne euch wäre ich nicht – wo ich bin, was ich bin, wie ich bin oder überhaupt. Danke, dass ihr mir immer jeden Weg offengehalten habt auch wenn er mal auf Klippen zulief. *Wolfgang*, du bist immer bei mir. Danke *Ursel*, dass du jederzeit für mich da oder einen Schritt voraus bist.

Erklärung

Ich versichere, dass ich diese Arbeit selbstständig verfasst und keine anderen als die angegebenen Quellen und Hilfsmittel benutzt habe.

Heidelberg, den ...,